PAPER
Ifan E. L. Stephens, Yu Katayama *et al.*
In situ spectroscopy reveals how water-driven SEI formation
controls selectivity in Li-mediated N_2 reduction

PAPER

Check for updates

In situ spectroscopy reveals how water-driven SEI formation controls selectivity in Li-mediated N$_2$ reduction†

Matthew Spry,[ac] Johannes Rietbrock,[a] Olivia Westhead,[a] Craig Burdis, ID [a] Cindy Tseng,[a] Asuka Morinaga,[c] James O. Douglas, ID [a] Michele Shelly Conroy,[a] Yasuyuki Kondo,[c] Yuki Yamada, ID [c] Maria-Magdalena Titirici, ID [b] Ifan E. L. Stephens*[a] and Yu Katayama ID *[c]

Understanding the fundamental processes that govern the formation of the solid electrolyte interphase (SEI) layer in lithium mediated nitrogen reduction is crucial to the design of improved electrolyte formulations. In this work, the roles of water and ethanol on the formation of the SEI are studied using *in situ* infrared spectroscopy and postmortem cross-sectional microscopy. Our results connect the observed SEI morphologies to specific observed SEI formation mechanisms. We directly detect formation of lithium ethoxide (LiEtO) as a major SEI component at potentials positive of Li plating when ethanol is used as the proton donor, which further reacts to form LiOH and Li$_2$O depending on water availability, and regenerates ethanol. We show that in water-containing electrolytes, the SEI consists of a highly porous outer layer, which we propose is largely LiOH, and a denser inner layer, consisting largely of Li$_2$O. We show that the water concentration relative to the ethanol concentration in the electrolyte can strongly influence the porosity of the SEI, which in turn influences N$_2$ reduction selectivity. Furthermore, our combined approach of directly probing SEI formation in real time and measuring morphological changes to the SEI can provide a framework for more informed SEI engineering to unlock further optimisation of the Li-mediated system.

Broader context

Ammonia is an essential feedstock chemical for agricultural fertilisers, but its conventional manufacture *via* the Haber–Bosch process contributes more than 1% of the world's total CO$_2$ emissions. Achieving net-zero global CO$_2$ emissions necessitates low-carbon ammonia production. A more sustainable method is electrochemical nitrogen reduction, which could enable decentralized production using renewable electricity. Among emerging approaches, the lithium-mediated system is the most developed. While rapid advances in ammonia selectivity have been made, understanding of what governs such selectivity has lagged behind. In particular, the solid–electrolyte interphase (SEI), which is thought to control the transport of species to the electrode surface, is poorly understood. This study demonstrates combined *in situ* infrared spectroscopy and postmortem microscopy to link observed initial SEI forming reactions to the final SEI structure and composition. It sheds new light on how ethanol as the proton source dominates the initial stages of SEI formation, and how it interacts with trace water at the electrode to form further SEI components such as LiOH and Li$_2$O. Moreover, this approach could form an integral part of future SEI engineering.

Introduction

Ammonia is one of the world's most important commodity chemicals, serving as a major feedstock to produce fertilisers.

[a] Department of Materials, Imperial College London, London, UK.
  E-mail: i.stephens@imperial.ac.uk

[b] Department of Chemical Engineering, Imperial College London, London, UK

[c] SANKEN (Institute of Scientific and Industrial Research), The University of Osaka, Ibaraki, Japan. E-mail: yuktym@sanken.osaka-u.ac.jp

† Electronic supplementary information (ESI) available. See DOI: https://doi.org/10.1039/d5ee01961c

Conventional ammonia synthesis *via* the Haber–Bosch process contributes more than 1% of global carbon emissions[1] and requires large-scale facilities operating at high temperatures and pressures, which restricts the ability of developing countries or remote areas to produce fertilisers. As a low-carbon, decentralized alternative, electrochemical ammonia synthesis powered by renewable energy offers the potential to revolutionize fertiliser production.[2] The most advanced and extensively researched electrochemical method is the lithium-mediated system. Since the verification of lithium-mediated ammonia synthesis in 2019,[3] dramatic improvements in key performance

8414 | *Energy Environ. Sci.*, 2025, **18**, 8414–8429

This journal is © The Royal Society of Chemistry 2025

metrics have been achieved, and the best-performing systems demonstrate commercially promising ammonia production rates, compared to other alternative N_2 reduction processes.[4] All successful improved systems follow the same essential formula: a lithium salt in an aprotic organic solvent, containing an organic proton source or a proton shuttle. At extreme negative potentials, Li electroplates on the electrode; this cleaves the dinitrogen triple bond to form Li_3N, which can then be protonated to ammonia.[5–9] Competing with nitrogen reduction are several parasitic side reactions, most notably hydrogen evolution, excess Li plating, and reduction of electrolyte components.[5,7,10–12]

One of the key strategies employed to optimise this system has been engineering of the solid–electrolyte interphase (SEI) layer, which forms on the electrode from electrolyte decomposition products and protects the electrolyte from further reduction.[10,11,13,14] This SEI is similar to that formed in lithium-ion batteries, which is lithium ion conductive but electrically resistive. The SEI typically forms on a battery's first charging cycle and provides a passivating barrier that prevents further electrolyte degradation.[15,16] However, in Li-mediated N_2 reduction, the SEI must permit transport of N_2 and protons, and can grow or change in composition and morphology over time, depending on the electrolyte conditions.[17–20] The term "SEI" will be used hereafter to refer collectively to deposits on the cathode during the initial potential scan and those formed during sustained operation. Based on theoretical models, it is generally assumed that controlling the transport rate of protons to the working electrode is crucial to achieving high-selectivity N_2 reduction instead of H_2 evolution,[7,21] and many reports credit the SEI as the reason for the high selectivity observed in this system.[11,13,14,17,18,20,22,23] Furthermore, the porosity of the SEI has been directly tied to its role in selectivity to ammonia,[11,18] which likely depends both on its composition and mechanism of formation.[17,18] The porosity of proton donor-derived SEI phases has been proposed to contribute to the selectivity in the Li-mediated system.[17,18,24] Therefore, in short, the SEI with optimal composition and structure should be permeable enough to allow transport of dissolved N_2 to reach the active surface, and it should restrict transport of protons or proton carriers and Li ions to enable ammonia synthesis but preventing excessive H_2 evolution and Li plating.

The proton donor's influence on the SEI composition and structure makes its role more complex than simply shuttling protons from the counter electrode (anode) to the working electrode (cathode). Many reports have suggested that the lithium mediated system does not generate ammonia in the absence of ethanol, the most commonly used proton donor.[5,6,17,18,25,26] However, Mygind et al. have proposed that ethanol is necessary for SEI formation, but is not necessary for nitrogen reduction once the SEI is formed, and that other electrolyte species are able to shuttle protons to the cathode.[27] Lazouski et al. proposed that the proton donor plays a major role in the permeability of the SEI and therefore the diffusion rates of N_2, Li^+ and the proton donor to the active surface,[18] with the SEI acting as an additional diffusional boundary layer. Further to this, McShane et al. reported that proton donor-derived alkoxides make up the majority of the SEI using different alcohols in a $LiClO_4$-based electrolyte, and suggested that the thickness of the alkoxide layer increases to a plateau where it regulates a steady transport of both the proton donor and Li^+ to the electrode surface.[19,28,29] Recent work from our own group using a $LiNTf_2$-based electrolyte observed via scanning electron microscopy that the SEI becomes thinner and more homogeneous with increasing EtOH concentration, as well as creating a more Li_2O and LiOH-rich SEI.[30]

These studies have revealed the crucial role the proton donor plays in both SEI composition and its morphology.[17,18,31] However, when ethanol is used as the proton source, the detection of lithium ethoxide in the SEI is not consistent.[14,17,19] Sazinas et al. detected small amounts of LiEtO alongside polyTHF in O_2 dosed electrolytes using NMR and GC-MS,[14] which differs from the alkoxide-rich SEI observed by McShane et al.[19] Our own XPS characterisation does not definitively identify LiEtO with certainty due to a lack of available reference data and the difficulty in accurately fitting O 1s and Li 1s core levels. TOF-SIMS measurements also do not detect LiEtO with certainty, as it could easily fragment into other species.[26,30] Due to the high reactivity of LiEtO and its solubility in THF, a LiEtO-rich SEI may degrade rapidly during sample preparation and transfer for postmortem characterisation measurements. It is likely that during long-term electrolysis, the LiEtO content of the SEI is in dynamic equilibrium of LiEtO formation from EtOH reduction and LiEtO dissolution or further reaction.[17,18] Aside from primary alcohols, proton shuttle species such as phenol with a lithium phenoxide buffer,[28] and a phosphonium ion[29] have been demonstrated to be highly active towards ammonia synthesis, but the role that these species play in SEI formation has not been studied in detail.

The crucial role of the lithium salt in both SEI composition and its morphology has also been discussed previously. In $LiClO_4$-containing electrolytes, LiCl, Li_2O and LiOH have been detected as major inorganic compounds based on X-ray photoelectron spectroscopy (XPS) and time-of-flight secondary ion mass spectrometry (TOF-SIMS) measurements,[11,13,26] while in electrolytes with fluorinated salts such as $LiBF_4$ or $LiNTf_2$, LiF has been detected as the major inorganic compound.[11,32] In long-term flow cell studies, Fu et al. found $LiBF_4$ electrolytes to significantly outperform $LiNTf_2$ and $LiClO_4$ due to forming a stable, compact SEI layer compared to $LiClO_4$ and avoids production of LiS_x species from NTf_2^- degradation that can poison the anode and cause excessive solvent oxidation.[33] Li et al. reported an improvement in faradaic efficiency at elevated pressure by dosing the N_2 gas stream with small amounts of O_2 in a $LiClO_4$ electrolyte, which corresponded to an increased amount of Li_2O in the SEI.[13] Our group reported a similar phenomenon in which the faradaic efficiency increased drastically with the addition of small amounts of water to electrolytes containing $LiClO_4$.[22] Note that the improvement in faradaic efficiency with the addition of water has only been demonstrated in the $LiClO_4$ system, and has a detrimental effect on

performance in several other reports, all of which use F-containing salts.[25,34,35] It is not clear from the literature whether the addition of O_2 would have the same effect in F-containing electrolytes, or whether this difference is unique to water.

Nonetheless, given its ubiquity as a contaminant, and its formation as a byproduct during N_2 reduction,[10,13] systems that can tolerate water would be highly preferable. Water oxidation would also provide a desirable anode reaction which would circumvent the need to oxidise H_2 derived from water splitting and would necessitate a water-tolerant cathode reaction. Water oxidation at the anode has been demonstrated using a separate aqueous anolyte[36] but not yet in the same organic electrolyte, which would present significant challenges. The role and effects of water on the composition and morphology of the SEI, and likely therefore the N_2 reduction selectivity, remain largely unexplored. Furthermore, despite numerous reports of postmortem SEI characterisation and *in situ* SEI formation,[19,20,37] there is little mechanistic understanding of the fundamental electrochemical reactions that govern it. Just as understanding SEI formation has been crucial to the development of improved electrolyte formulations in lithium-ion batteries, so too could understanding the SEI in N_2 reduction prove essential to future development. Given that the active surface and some SEI components are highly reactive, *ex situ* SEI characterisation methods do not necessarily capture the operating conditions during ammonia formation or the process of SEI formation itself. *In situ* characterisation of the SEI can provide far greater insight into the processes that govern SEI structure, composition and performance.

In this report, we employ *in situ* Fourier transform infrared (FTIR) spectroscopy to detect key SEI-forming reactions at different ethanol and water concentrations during an initial cathodic voltage scan towards the Li plating potential. We relate these reactions to the morphology of SEI cross-sections observed using postmortem scanning electron microscopy, to link electrolyte composition and initial SEI-forming reactions to the final SEI structure and morphology. We employ the same microscopy method as another recent work from our group, which investigated the effects of ethanol on the SEI in LiNTf$_2$-containing electrolytes.[30] In contrast, this work focuses on LiClO$_4$-based electrolytes, as we have previously demonstrated that water can improve the selectivity of this system. To better understand our previous results, we focus in particular on the relationship between water and ethanol content in the electrolyte, and how reaction mechanisms involving these species govern the structure of the resulting SEIs.

Results

In situ FTIR measurements

Fig. 1a shows the FTIR spectra measured on an initial cathodic sweep from open circuit potential towards Li plating in an electrolyte consisting of 1 M LiClO$_4$ in THF with 0.17 M (1 vol%) ethanol and 2.5 mM (45 ppm) water. This corresponds to nominally dry conditions, without added water, to firstly understand the role of ethanol.

All spectra shown are relative to a background spectrum measured at open-circuit potential prior to any electrochemical measurements and therefore contains absorption from the bulk electrolyte. All positive peaks represent an increase in IR absorption relative to open circuit potential, and negative peaks a decrease in IR absorption relative to open circuit potential. From the open circuit potential (approx. +3.4 V_{Li/Li^+}) to around +2.0 V_{Li/Li^+}, the growth in the absorption bands at 1040 cm^{-1} and the downwards band at 1068 cm^{-1} represents a change in the absorption frequency of ring-stretching of THF during charging of the electrochemical double layer. This reflects the decrease in the local concentration of free and Li-coordinated THF and increase in local concentration of THF in solvent-separated ion pairs (SSIPs) or contact-ion pairs (CIPs) near the working electrode surface, as discussed in our previous work.[26,38] Between +2.0 V_{Li/Li^+} and +1.7 V_{Li/Li^+}, an increase in intensity of absorption bands from the bulk electrolyte is observed corresponding to feature 1 on the CV in Fig. 1c, which may arise from the reduction of copper oxides. The peak does not appear significantly using Cu foil under the same conditions, probably due to the larger roughness of Cu SEIRA surface compared to the Cu foil surface. This coincides with the appearance of interfacial water in the IR spectra at 1600 cm^{-1} (H–O–H bending) and 3200–3500 cm^{-1} (O–H stretching), which is not detectable in the bulk electrolyte IR spectrum at such low concentration. This suggests accumulation of trace water at or near the electrochemical interface as the potential is decreased. One possible explanation is the favourable migration of Li$^+$ ions with smaller, H$_2$O-containing solvation shells towards the electrode, compared to Li$^+$ ions surrounded only by bulkier THF molecules and anions.

Beginning at around +1.1 V_{Li/Li^+} and corresponding to feature 2 on the CV in Fig. 1b, prominent bands arise at 2811 cm^{-1}, 2707 cm^{-1}, 1382 cm^{-1}, and 887 cm^{-1}. By comparing with reference spectra of a pure sample in an Ar glove box, we confirm that these bands correspond to solid lithium ethoxide, as shown in Fig. 1a (bottom). We assign feature 2 in Fig. 1c to the following reaction:

$$\text{EtOH} + \text{Li}^+ + e^- \rightarrow \frac{1}{2}\text{H}_2 + \text{LiEtO} \qquad (1)$$
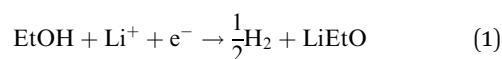
Simultaneously, the down-going bands from THF indicate the displacement or blocking of THF from the working electrode surface by the formation of lithium ethoxide. Other strong bands from lithium ethoxide occur around 1050 and 1124 cm^{-1}, however these may overlap with C–O stretching from THF and ethanol, and Cl–O stretching from the perchlorate ion respectively.[26,39,40] In experiments using LiNTf$_2$ as the salt, the same blocking of the working electrode with a layer of LiEtO is observed (Fig. S10b, ESI†). Characteristic absorption bands for Li$_2$CO$_3$ at 1445 cm^{-1} and 1500 cm^{-1},[41] and poly(THF) between 1200–1500 cm^{-1},[42] were not observed in any of these experiments. The poly(THF) observed in other reports *via* postmortem characterisation[10,14] likely results from THF electro-oxidation at the anode followed by in solution chemical polymerisation,[43,44] which later deposits on the working

8416 | *Energy Environ. Sci.*, 2025, **18**, 8414–8429

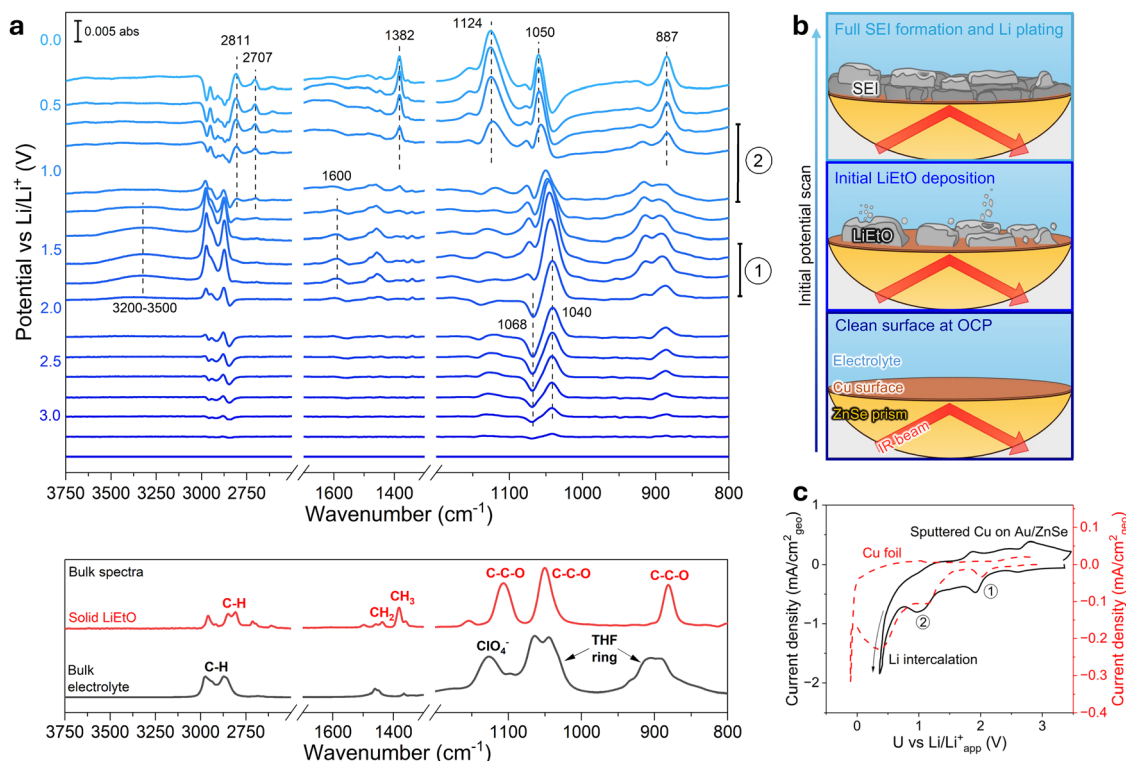This journal is © The Royal Society of Chemistry 2025

Fig. 1 (a) FTIR spectra of the working electrode during the initial SEI-forming cathodic potential scan from OCP towards the apparent Li plating potential, in an electrolyte of 1 M $LiClO_4$ in THF with 0.17 M ethanol as a proton donor and 2.5 mM (45 ppm) water. The working electrode consists of a 50 nm sputtered Cu film on top of an Au adhesion layer deposited on a 22 mm diameter hemispherical ZnSe prism. The background spectrum was taken at OCP and subtracted from each subsequent spectrum. Spectra are positioned to intersect the *y*-axis at the potential at which they were measured. Reference spectra for bulk electrolyte and pure solid LiEtO were measured using a diamond ATR accessory inside an Ar glove box (b) Schematic showing the initial stages of SEI formation on the Cu on a ZnSe prism electrode setup during the first potential scan. (c) CV of the first cycle at a scan rate of -5 mV s^{-1} (black line) and compared to the same conditions on Cu foil in a similar cell (red dashed line). Working electrode potential is corrected for Ohmic drop ($R_{U,FTIR} = 120\ \Omega$, $R_{U,foil} = 110\ \Omega$). The IR cell is a single compartment with a 1 cm^2 Pt mesh counter and Pt wire reference, each with approximately 1 cm separation (Fig. S1, ESI†).

electrode. Species such as Li_2O and LiCl have been observed in postmortem XPS under these conditions,[13,14,22,26] but are IR inactive so would not be detected here. Therefore, *in situ* FTIR observation implies that LiEtO and IR-inactive species (such as Li_2O or LiCl) must be the major SEI components just before the onset of Li plating. Detailed peak assignments and reference spectra for observed species can be found in the ESI† (Fig. S6–S8).

Effects of ethanol concentration

As the formation of LiEtO clearly dominates the SEI initially using 0.17 M ethanol in the electrolyte, the influence of ethanol was further investigated using different ethanol concentrations. The *in situ* IR spectra in the C–H stretching region in electrolytes containing 0 M, 0.17 M and 0.51 M ethanol (0, 1 and 3 vol%) are shown in Fig. 2a. A comparison of the wider spectra measured near Li plating potential is shown in Fig. 2b. For all three ethanol concentrations, the trends in IR spectra are very similar down to approximately +1.5 V_{Li/Li^+} showing the same changes in double layer composition (Fig. S10 and S11, ESI†). Characteristic bands for LiEtO are clearly observed below +1.1 V_{Li/Li^+} in both ethanol-containing electrolytes.

In the absence of ethanol, bands from bulk electrolyte at 2973, 2875 and 1040 cm^{-1} (THF) and 1128 cm^{-1} (ClO_4^-) decrease in intensity and eventually become down-going between +0.5 and 0 V_{Li/Li^+}. This indicates that an impermeable SEI layer forms which blocks bulk electrolyte from the electrode surface. As no significant positive IR absorption bands are observed in these spectra, the most likely candidates for dominant SEI species are IR-inactive species like LiCl from the reduction of the ClO_4^- ion, as reported in our previous work,[26] or Li_2O. As expected, the characteristic peaks for LiEtO at 2808 cm^{-1}, 2713 cm^{-1} and 1382 cm^{-1} are not observed in the absence of ethanol, further supporting our peak assignment. Similar SEI formation behaviour is initially observed from the FTIR spectra using 1 M LiNTf$_2$ as the salt in the absence of ethanol, shown in Fig. S10a (ESI†), in which all observable absorption bands around Li plating potential can be ascribed to bulk electrolyte.

In the electrolyte containing 0.51 M ethanol, we expect a negligible amount of ammonia to form, based on previous reports which attribute this to excessive H$_2$ evolution due to high proton activity.[5,6,25] Note that the appearance of LiEtO in this case is not accompanied by a significant decrease in band

This journal is © The Royal Society of Chemistry 2025

Energy Environ. Sci., 2025, **18**, 8414–8429 | **8417**
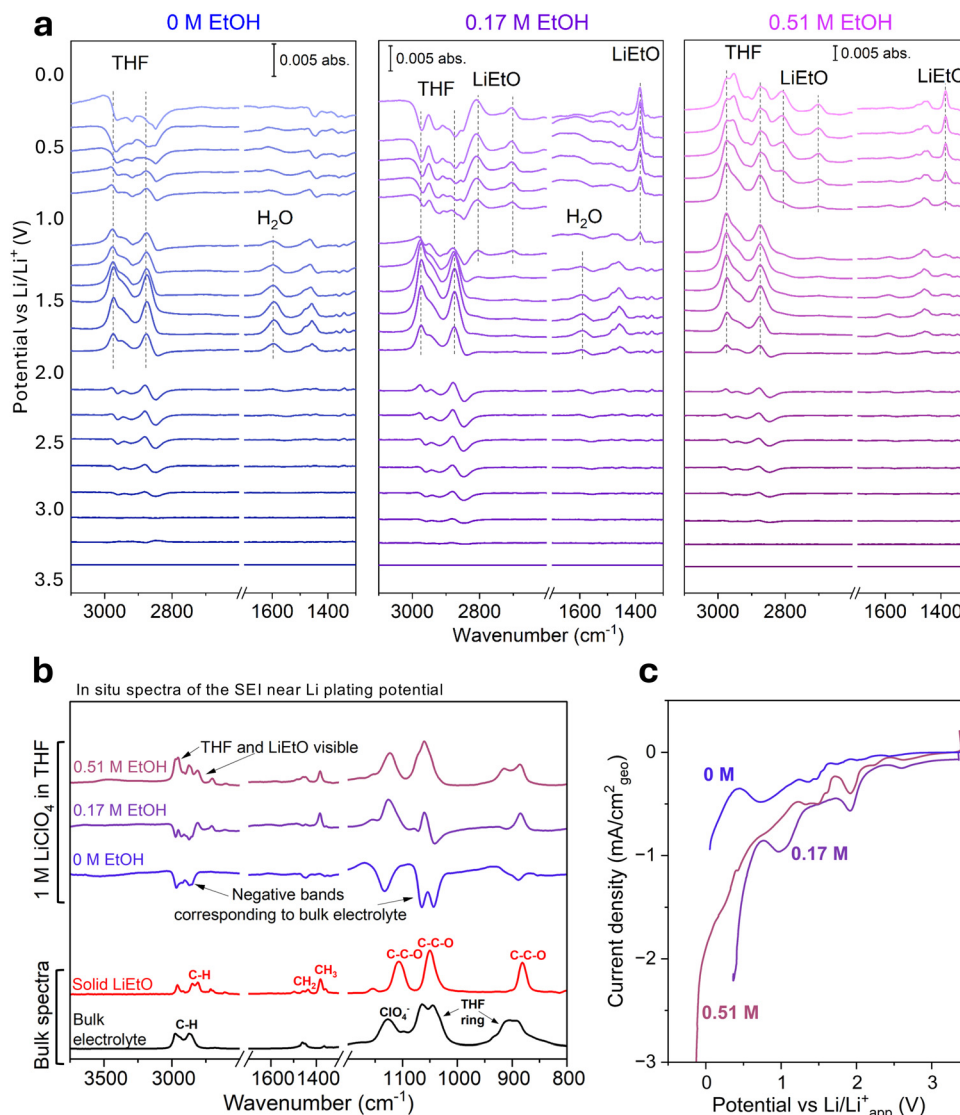
Fig. 2 (a) FTIR spectra of the working electrode during the initial SEI-forming cathodic potential scan from OCP towards the apparent Li plating potential in an electrolyte consisting of 1 M $LiClO_4$ in THF with 0 M, 0.17 M and 0.51 M ethanol (0%, 1% and 3% by volume), and < 2.5 mM (∼45 ppm) water. The working electrode consists of a 50 nm sputtered Cu film on top of an Au adhesion layer deposited on a 22 mm diameter hemispherical ZnSe prism. Spectra are all relative to a background spectrum taken at the initial OCP. (b) Comparison of the spectra measured closest to 0 V_{Li/Li^+} in each case with measured ATR spectra of the bulk electrolyte and solid LiEtO for reference. (c) LSVs measured in electrolytes of 0 M, 0.17 M and 0.51 M ethanol at a scan rate of −5 mV s^{-1}. Working electrode potentials are corrected for Ohmic drop (R_U = 120 Ω). The IR cell is a single compartment with a 1 cm^2 Pt mesh counter and Pt wire reference, each with approximately 1 cm separation (Fig. S1, ESI†).

intensities from bulk electrolyte. The observation could either indicate that the SEI becomes thin enough that electrolyte remains within the IR penetration depth, or that the SEI becomes porous enough that electrolyte is able to reach the electrode surface. Considering that the LSV for the 0.51 M ethanol experiment (Fig. 2c) shows continuously increasing current between the onsets of LiEtO formation and Li plating, we propose that the porosity of the SEI layer was increased in 0.51 M ethanol system, as it does not inhibit further ethanol reduction and H_2 evolution. Our hypothesis is in line with the observation of Lazouski *et al.*[18] and Blair *et al.*,[20] further supporting the formation of porous SEI with relatively high proton donor concentration.

The contrast between the surfaces of the working electrodes around Li plating potential can be seen most clearly in Fig. 2b. In the 1000–1200 cm^{-1} wavenumber region, negative bands from THF and the ClO_4^- ion are present in the 0 M ethanol experiment. Bands corresponding to LiEtO are most prominent again in the 0.17 M ethanol experiment with negative bands from THF, and bands from both LiEtO and THF can be seen in the 0.51 M experiment.

Effects of water

The presence of water in the electrolyte has been shown to dramatically affect SEI composition and N_2 reduction performance, both positively and negatively, even at very low

8418 | *Energy Environ. Sci.*, 2025, **18**, 8414–8429

This journal is © The Royal Society of Chemistry 2025

concentrations.[9,22,25,45] To better understand the effects of water on SEI formation, we use a combined approach of measuring the chemical composition of the SEI using *in situ* FTIR spectroscopy (Fig. 3) and the surface morphology using postmortem cryo-SEM (Fig. 5). Due to the difficulty of precisely reproducing the water concentration at such small values, the water concentrations used to prepare the samples for cryo-SEM measurements differ slightly from those in the FTIR experiments. However, they can be broadly classified as dry (<3 mM, 50 ppm), medium (35–40 mM, 650–750 ppm) and high (>90 mM, 1700 ppm) water concentrations, based on our previous work which found a local maximum in faradaic efficiency to ammonia in $LiClO_4$ electrolytes in the range of 36–43 mM (650–770 ppm) with a salt concentration of 0.8 M.[22] The water concentration ranges tested herein correspond to faradaic efficiencies of around 3% (dry), 20% (medium water) and $<1\%$ (high water), based on batch cell experiments passing 10C of charge at -2 mA cm^{-2}.[22]

In the dry $LiClO_4$ system, the Li plating appears completely irreversible under potential cycling, both during an initial cycle at 5 mV s^{-1} and during subsequent 20 mV s^{-1} cycles (Fig. S4, ESI†) which indicates a poorly passivating SEI layer. At increasing water concentrations, the Li deposition rates remain similar on the first CV cycle (Fig. S4a, ESI†). However after six potential cycles (Fig. S4b, ESI†), the Li deposition rate significantly decreases with increased water concentration, approximately 40% lower with 40 mM water and 85% lower with 100 mM. Additionally the stripping efficiency (SE) of Li increases with increasing water concentration. After six potential cycles around Li plating potential, in the medium water concentration electrolyte, approximately 7% of the electrodeposited Li is oxidised, which increases to 38% in the high water concentration electrolyte. This indicates that the increased water concentration creates a more passivating SEI layer which provides a barrier to both Li plating and to the corrosion of electrodeposited Li. This is in qualitative agreement with Li
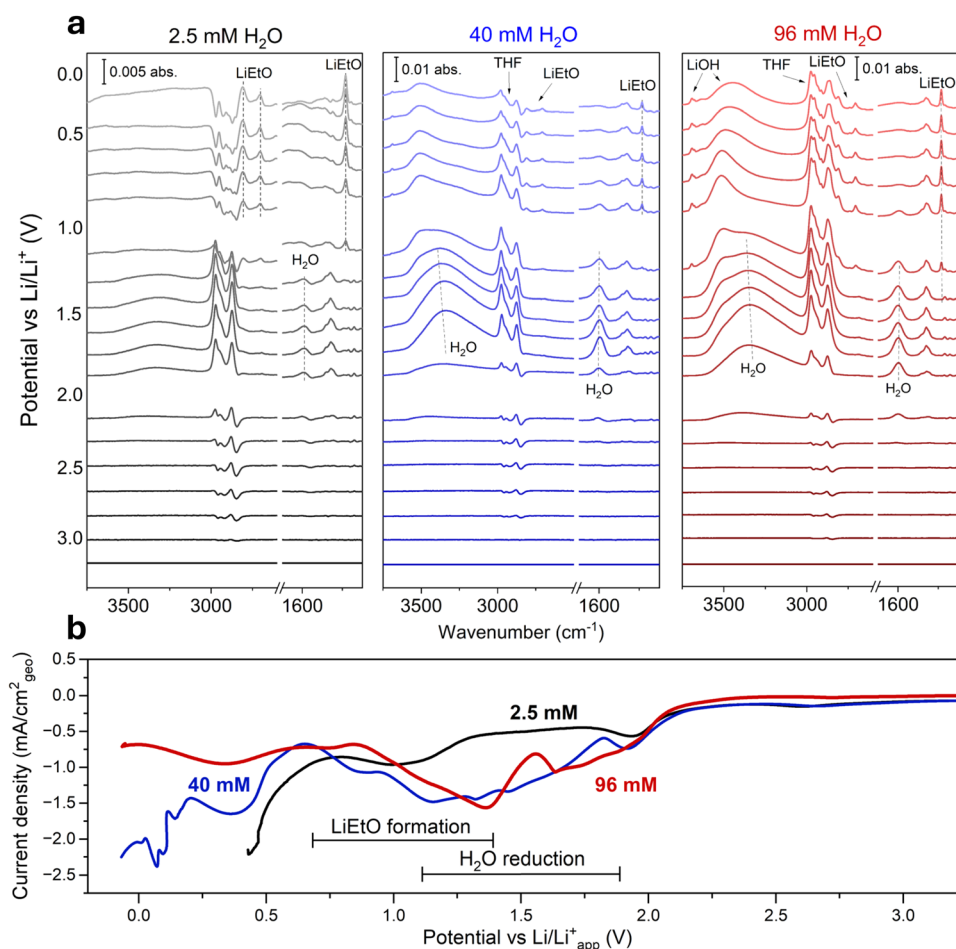

Fig. 3 (a) FTIR spectra of the working electrode during the initial SEI-forming cathodic potential scan from OCP towards the apparent Li plating potential obtained in an electrolyte of 1 M $LiClO_4$ in THF with 0.17 M ethanol (1% by volume) and 2.5 mM (45 ppm), 40 mM (750 ppm) and 96 mM (1760 ppm) water. The working electrode consists of a 50 nm sputtered Cu film on top of an Au adhesion layer deposited on a 22 mm diameter hemispherical ZnSe prism. Spectra are all relative to a background spectrum taken at the open circuit potential at the beginning of the experiment (approx. $+3$ V *vs.* Li/Li$^+$). (b) LSVs measured in electrolytes of 2.5 mM, 40 mM and 0.96 mM water with 0.17 M ethanol at a scan rate of -5 mV s^{-1}. Working electrode potentials are corrected for Ohmic drop ($R_U = 120$ Ω). The IR cell is a single compartment with a 1 cm^2 Pt mesh counter and Pt wire reference, each with approximately 1 cm separation (Fig. S1, ESI†).

This journal is © The Royal Society of Chemistry 2025

Energy Environ. Sci., 2025, **18**, 8414–8429 | **8419**

metal battery studies by Koshikawa *et al.* The low Li$^+$ ionic conductivity of Li$_2$O and LiOH in the SEI layer are most likely responsible for the suppressed Li deposition rates at higher water concentrations, which may contribute to the improvement in selectivity by suppressing excessive Li plating. The similar rates of Li deposition on the first cycle at different water concentrations (Fig. S4a, ESI†) implies this passivating layer is not fully formed on the first cycle, but likely grows during sustained operation.

FTIR spectra from the initial cathodic scans in electrolytes with dry, medium and high water concentrations are shown in Fig. 3.

In experiments with dry electrolytes (water concentration below 50 ppm), interfacial water was clearly observed near the working electrode at potentials below +2 V_{Li/Li^+} (Fig. 3a), which is not visible in the bulk electrolyte spectrum at such concentrations without an applied potential. Even trace amounts of water in the electrolyte may thus have a strong influence on SEI formation if it disproportionately accumulates at or near the working electrode. This is consistent with reports from Strmcnik *et al.* concerning the fate of water impurities in lithium-ion batteries, in which Li$^+$ in the double layer forms a Li$_2$–H$_2$O complex and facilitates the dissociation of water.[46–48] While our previous report found that water can enhance the faradaic efficiency dramatically in LiClO$_4$-based systems, further experiments conducted since have shown poor long-term performance (Fig. S4, ESI†) which is the subject of ongoing study.

With the medium water concentration, the broad bands from 3200–3500 cm^{-1} and 1600 cm^{-1} from interfacial water appear at around +2.0 V_{Li/Li^+} with similar intensity to those peaks from THF, providing further evidence of locally high water concentration at the electrode surface. Between the appearance of interfacial water and the onset of LiEtO formation around +1.1 V_{Li/Li^+}, we observe narrowing of the band in the O–H stretching region and its shift to higher wavenumbers that occurs slightly above +1.4 V_{Li/Li^+} which indicates greater isolation of water molecules or breaking of hydrogen bonds.[49] This likely involves the reduction of water to OH$^-$ and H$_2$, as it coincides with the large reductive feature on the LSVs (Fig. 3b). A small, sharp peak at 3692 cm^{-1} observed around +1.1 V_{Li/Li^+} is attributed to O–H stretching in solid crystalline LiOH (Fig. 4). The broader peak centred around 3500 cm^{-1} is attributed to hydrated LiOH.[50,51] In line with the formation of LiOH from +1.1 V_{Li/Li^+}, the sharp reduction in peak intensity of the H–O–H bending peak from water at 1600 cm^{-1}, which indicates the consumption of interfacial water to form LiOH. At around +1.1 V_{Li/Li^+} where LiEtO formation begins, the C–H stretching bands from THF decrease in intensity. The signals do not become down-going bands, indicating that THF is only partially blocked from reaching the electrode.

Similar potential dependent change in the spectra were observed in the high water concentration; locally high water concentration at the electrode surface at around +2.0 V_{Li/Li^+} and subsequent isolation of water molecules or breaking of hydrogen bonds at above +1.4 V_{Li/Li^+}, solid crystalline and hydrated LiOH formation, and LiEtO formation from +1.1 V_{Li/Li^+}.
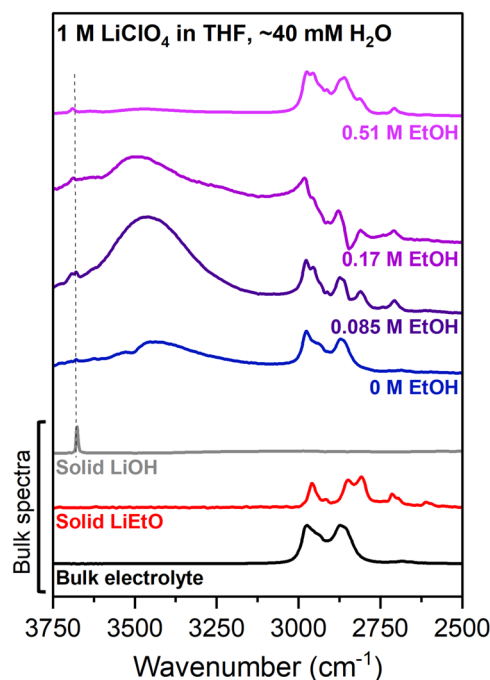

Fig. 4 Comparison of the *in situ* FTIR spectra of the SEIs taken near Li plating potential in electrolytes of 1 M LiClO$_4$ in THF containing approximately 40 mM water (medium concentration) with ethanol concentrations of 0, 0.085, 0.17 and 0.51 M, corresponding to 0%, 0.5%, 1% and 3% ethanol by volume respectively. All spectra are relative to spectra measured at the initial open circuit potential in each experiment (approx. +3.3 V *vs.* Li/Li$_{app}^+$). The bulk spectra of the electrolyte and pure LiOH and LiEtO were measured using an ATR accessory inside an Ar glove box.

Note that the measurements from both LiClO$_4$ and LiNTf$_2$ electrolytes (Fig. S10 and S11, ESI†) are consistent with a passivating inorganic, IR-inactive and therefore mostly salt-derived SEI layer forming in the absence of ethanol beginning around +1.1 V_{Li/Li^+}, which blocks access of the electrolyte to the surface. In ethanol-containing electrolytes, the formation of LiEtO also occurs around 1.1 V_{Li/Li^+}, so too does formation of crystalline LiOH at higher water concentrations. The coincidence of these reactions indicates a common process that facilitates or catalyses breakdown of the salt anion and reduction of ethanol. One possible explanation is the underpotential deposition (UPD) of Li onto Cu, which has been observed around +0.6 V_{Li/Li^+} and theorised *via* DFT calculations at +1 V_{Li/Li^+} on Cu(111) and Cu(100).[52,53] Alternatively, these SEI-forming reactions may be driven by the accumulation of Li$^+$ into the double layer and adsorption of Li$^+$ onto the electrode surface, as observed in Li-ion batteries by Strmcnik *et al.* on Cu, Au and Pt.[46,47] Additionally, recent findings show that the presence of Ag salts in the electrolyte can enhance ammonia selectivity be mediating Li deposition, which could also strongly influence SEI formation.[54] Both interpretations would imply that the process of SEI formation under a potential sweep could differ depending on the electrode material.

Further comparison of the spectra with different water concentration reveal that the IR band intensities from LiEtO

8420 | *Energy Environ. Sci.*, 2025, **18**, 8414–8429

This journal is © The Royal Society of Chemistry 2025

are significantly lower in experiments with added water, as well as the peaks associated with both crystalline and hydrated LiOH are more intense. The above observation is likely due to the rapid consumption of LiEtO to form Li_2O and LiOH via the reactions:

$$LiEtO + H_2O \rightarrow LiOH + EtOH \qquad (2)$$

$$LiEtO + \frac{1}{2}H_2O \rightarrow \frac{1}{2}Li_2O + EtOH \qquad (3)$$
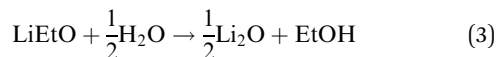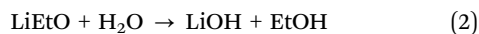
This is corroborated by postmortem XPS measurements which also indicate high LiOH and Li_2O content in the SEI in water-containing electrolytes (Fig. S3, ESI†), which can be explained by reactions (2) and (3). At higher water concentrations, reaction (2) would contribute to the increase in LiOH, as well as direct reduction of H_2O in the presence of Li^+ ions. The further reaction of Li_2O with water (eqn (4)) likely also contributes to LiOH formation.

$$Li_2O + H_2O \rightarrow 2LiOH \qquad (4)$$

However, the enhancement of the faradaic efficiency with added water does not appear to be a long-term phenomenon. In a 12-hour electrolysis experiment, the enhanced faradaic efficiency was observed to remain for around 2 hours of operation under medium water conditions, at an applied current density of -2 mA cm^{-2} (Fig. S5, ESI†). After around 2 hours, the faradaic efficiency dropped to around 15% then gradually decayed to approximately 0%. We attribute this behaviour to the excessive accumulation of LiOH in the SEI, which is poorly soluble in the electrolyte and unlikely to undergo further reaction under these conditions. This could be mitigated by changing the composition of the electrolyte after the initial stages of SEI formation, or developing an electrolyte in which LiOH better dissolves, which is an interesting avenue for further study.

The IR spectra measured at the onset of Li plating in electrolytes with medium (approximately 40 mM) water concentration with different ethanol concentrations are shown in Fig. 4. Full spectra for each experiment can be found in the ESI.† The intensity of IR bands from LiOH, at around 3500 cm^{-1}, relative to other bands are greatest for the electrolyte containing 0.085 M ethanol (0.5 vol%). These bands become considerably smaller as the ethanol concentration is increased, which may indicate that Li_2O produced by reaction (3) is favoured over LiOH via reaction (2). It is possible therefore that the ratio of Li_2O to LiOH in water-containing electrolytes is related to the relative concentrations of ethanol and water. For a high ethanol–water ratio, a Li_2O-rich SEI is favoured, and conversely if the ethanol–water ratio is low, a LiOH-rich SEI is favoured.

The bands associated with background electrolyte are also far greater relative to LiOH and LiEtO in the high water concentration experiment. This indicates that with added water, the SEI becomes either thinner or more porous, which enables more infrared absorption from the bulk electrolyte.

Discerning specifically how the influence of water affects porosity requires direct observation of the SEI's morphology.

Investigating SEI morphology with cross sectional microscopy

To relate the initial SEI formation FTIR measurements to long-term SEI and to test the hypothesis that water in the electrolyte increased the porosity of the SEI, cryogenic SEM measurements were made of SEI cross-sections. 10C of charge was passed at -2 mA cm^{-2} on Cu or Mo foil electrodes in 1 M $LiClO_4$ electrolytes with 0.17 M ethanol containing dry (2.5 mM (45 ppm)), medium (40 mM (750 ppm)) and high (96 mM (1760 ppm)) water, and one with 0 M ethanol and medium (40 mM (750 ppm)) water. XPS measurements were made on different sections of the same electrodes as those in the micrographs, shown in Fig. S8 (ESI†). As these micrographs show the SEI cross sections following chronopotentiometry, they likely do not have the same structure and composition at the time of measurement as the SEIs in the FTIR experiments. Rather, the IR measurements are used to determine the types of reaction that occur during initial SEI formation which could cause the structures and morphologies seen in the postmortem microscopy images.

Micrograph cross sections of the SEIs are shown in Fig. 5, displaying the full cross section (left), higher magnification of the cross section (centre) and a schematic representation of the higher magnification micrograph (right) to identify key regions of the SEI. The lighter sections of the micrographs represent species with higher atomic masses, as these elements cause a greater proportion of backscattered electrons; darker sections represent lighter elements. The Mo or Cu electrodes are visible as the lighter area below the SEI in each case.

In three of the samples, the micrographs show horizontal cracks across the SEI. Cracks could form during sample preparation, as two SEI phases with different thermal expansion coefficients would contract at different rates during cooling. Alternatively, they may have formed during electrolysis, after which they would likely fill with electrolyte. Below the crack in the SEI in Fig. 5a, e and i (dry electrolyte, 0.17 M EtOH), a mostly dense layer near the electrode surface is visible interspersed with small voids. The dark regions above the crack are likely deposits of "dead" lithium–metallic Li that has become passivated and is electrically isolated from the electrode. The broad white areas above these dead Li deposits suggest regions containing heavier elements than Li. In the SEI formed in this electrolyte, Cl is the largest major element by atomic mass, suggesting the possibility of deposits such as LiCl or other products derived from $LiClO_4$, as detected in our XPS measurements (Fig. S3, ESI†). Above the dead Li layer, the SEI exhibits a mosaic-like structure, with numerous phases of differing compositions, as indicated by the granular contrasting patches. This micrograph does not necessarily show a porous outer SEI layer, as we previously hypothesised. However, this layer likely contains more organic species, based on our group's prior findings using XPS and secondary ion mass spectrometry (SIMS).[26]
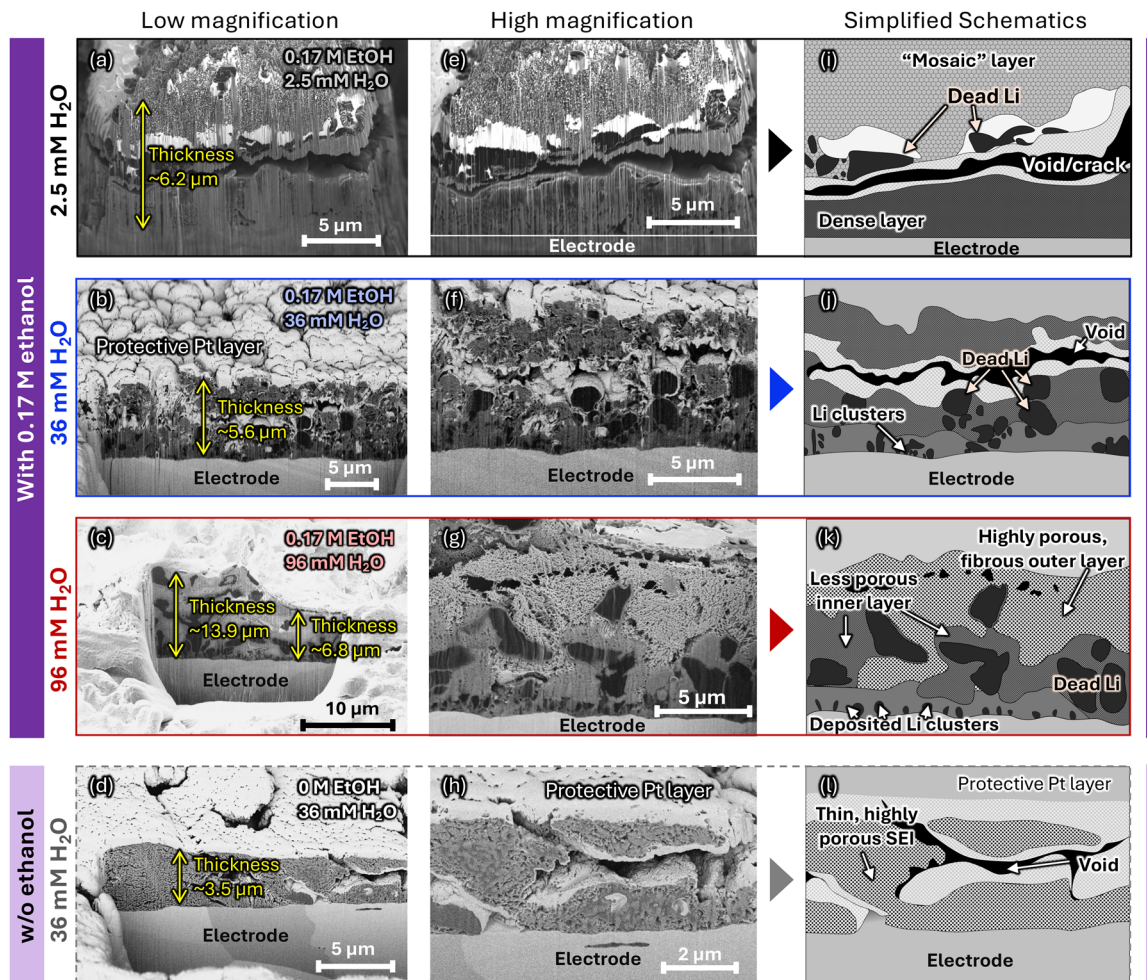
Fig. 5 SEM micrographs of SEI cross sections cut using FIB milling formed in electrolytes of 1 M LiClO$_4$ in THF with (a), (e) and (i) 0.17 M ethanol, 2.5 mM water; (b), (f) and (j) 0.17 M ethanol, 36 mM water; (c), (g) and (k) 0.17 M ethanol, 96 mM water; (d), (h) and (l) 0 M ethanol, 36 mM water, on Cu or Mo electrodes, each labelled with the observed SEI thicknesses. (e)–(g) Higher magnification images of each SEI cross-section. (i)–(l) Simplified SEI cross-section schematics with major SEI features labelled. The protective Pt later deposited on samples prior to FIB milling is seen as a white layer at the top of the samples. Each SEI was formed by passing 10C of charge at −2 mA cm^{-2} on a 1 cm^2 foil working electrode in an N$_2$-saturated electrolyte.

In the SEI formed under optimal water conditions (40 mM water), the boundaries between the SEI layers are less distinct compared to the SEI formed in a dry electrolyte. The large voids between dead Li clusters visible in the central part of this SEI cross-section are surrounded by lighter-coloured layers which imply this phase contains heavier elements than its surrounding, so may contain Cl-based species, resulting from ClO$_4^-$ reacting with Li. There are similarly-sized clusters of dead Li compared to the dry electrolyte SEI, however numerous small clusters near the electrode surface are visible which are surrounded by an apparently dense phase with few visible pores. This would suggest that the innermost phase of the SEI is highly passivating.

The high water concentration SEI (96 mM water) is significantly thicker than in the other samples but exhibits less uniformity, with thicknesses ranging from 6.8 μm to 13.9 μm across the cross-section. This SEI contains significantly more dead Li deposits. The SEI material between these deposits is more uniform compared to previous samples and can be divided into three distinct regions. The outer SEI layer consists of a porous, fibrous matrix surrounding the dead Li deposits. In the lower half of the SEI, a noticeable change in morphology occurs, with an apparently denser, less porous structure. The darker coloration of this lower layer suggests the presence of lighter species compared to the upper layer. Closer to the electrode, small, teardrop-shaped Li clusters span the electrode interface, which could indicate nucleation sites for Li deposition. At this proximity to the electrode, it is difficult to distinguish whether these clusters are dead Li or unreacted, electrically connected Li. The denser material in the lower layer seems to coat the dead Li deposits, indicating a higher degree of passivation.

In the absence of ethanol but with 38 mM water, the SEI is considerably thinner and contains large voids. The solid material appears as a single, highly porous phase, unlike the multilayered SEIs observed in other samples whilst visually

8422 | *Energy Environ. Sci.*, 2025, **18**, 8414–8429

This journal is © The Royal Society of Chemistry 2025

resembling the outer layer of the SEI observed with ethanol and 96 mM H_2O. Notably, there is no visible dead Li in this SEI, implying that the presence of ethanol in the electrolyte plays a key role in the passivation of Li, leading to the formation of large Li deposits.[53,54]

Discussion

By combining insights from *in situ* FTIR measurements of the initial stages of SEI formation with the cross-sectional microscopy images following electrolysis, we can propose several key mechanisms underpinning SEI formation, which are depicted in Fig. 6.

SEI formation in dry electrolytes

In the absence of water, SEI formation is initially dominated by LiEtO presumably alongside some IR-inactive species such as LiCl, Li_2O or LiF, depending on the salt anion and solvent. LiEtO will accumulate in the SEI until its dissolution or reaction rate equilibrates with its rate of formation, as observed by McShane *et al.*[19] Cross-sectional microscopy shows a dense layer near the electrode (Fig. 5a, e and i) which correlates with the absence of THF bands in the FTIR spectrum around Li plating potential, as this layer prevents THF from freely reaching the electrode surface. Additionally, the absence of IR bands corresponding to LiOH or $LiClO_n$ indicates that the main inorganic components of this layer initially are IR-inactive, making LiCl and Li_2O the most probable constituents alongside LiEtO.

While impossible to detect using FTIR, LiCl has been observed as a major SEI constituent in $LiClO_4$ based electrolytes using XPS,[26] and is formed from the reduction of the ClO_4^- anion. However, LiCl is partially soluble in THF,[55] which may lead to some SEI dissolution in $LiClO_4$-based systems. When using fluorinated salts like $LiBF_4$ or $LiNTf_2$, LiF is a major inorganic SEI component,[11,32] which has very low solubility in THF (maximum 0.09 mM at 24 °C).[56] The insolubility of LiF may partly explain the greater stability of the SEI, and the generally higher N_2 reduction performance observed using F-containing salts.[9–11,25]

SEI formation in water-containing electrolytes

The FTIR spectra around Li-plating potential indicated that increasing the water content of the electrolyte led to a more porous SEI, containing LiOH which allowed THF and $LiClO_4$ to reach the electrode. This increased porosity is evident in the micrographs of the SEIs formed in the absence of ethanol, and with high water concentration, in which highly porous SEI phases can be seen. The evolution of H_2 from the reduction of water may contribute to the increased porosity, as reported elsewhere,[17,18,57] or the faster dissolution of LiEtO from the SEI in the presence of water. Additionally, the presence of water has been shown to form non-passivating, porous LiOH in batteries.[58,59] The predominance of LiOH in the SEI would explain the lack of passivation and the corresponding absence of dead Li in the absence of ethanol. The similarity of the morphology of the SEI formed without ethanol to the porous outer layer seen in the high water content SEI suggests both primarily consist of LiOH, which is in agreement with surface XPS measurements on both samples (Fig. S3, ESI†). The stability of LiOH in THF, unlike many other ring-based organic solvents, further supports this interpretation.

In electrolytes containing both ethanol and water, a less porous, more passivating inner SEI layer forms, which is not observed in the absence of EtOH. This is most likely related to an interaction between LiEtO and water. As the FTIR does not
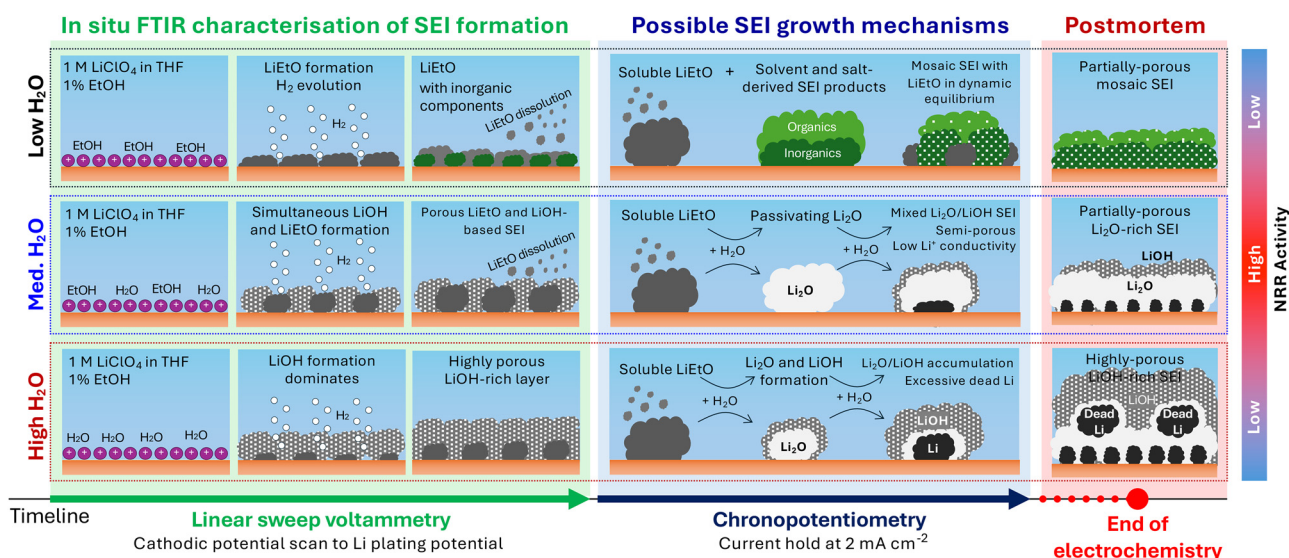

Fig. 6 (Left) Schematic of SEI components during initial SEI formation for different water concentrations and using ethanol as the proton donor, informed by our *in situ* FTIR measurements. (Middle) Proposed mechanisms for the restructuring and growth of the SEI during chronopotentiometry, which show the dissolution or transformation of the LiEtO phase into Li_2O or LiOH depending on the water concentration. (Right) Simplified schematic of the SEI structure observed after electrochemical measurements, informed by postmortem cryo-microscopy and XPS.

detect any additional IR-active species, we propose that this layer consists primarily of Li_2O with some LiOH. We hypothesise that Li_2O forms from the reaction between LiEtO and water (reaction (3)) when the availability of water is low relative to the amount of LiEtO. This mechanism may explain why electrolytes containing ethanol and water lead to the accumulation of significant amounts of dead Li, as Li_2O forms a more passivating and THF-insoluble layer. However, over time, we would expect further reaction between Li_2O and water to occur, generating LiOH. Like LiF, Li_2O exhibits very low solubility in most organic solvents,[60,61] so the formation of Li_2O in $LiClO_4$-based electrolytes may provide the stable, insoluble, passivating phase that is provided by LiF in electrolytes with F-containing salts, but that is not provided by LiCl.

Excessive water in the electrolyte or unrestricted access to the electrode likely promotes H_2 evolution coupled with LiOH. As the SEI becomes thicker over the course of chronopotentiometry, we expect that the porous LiOH phase is pushed outward as bulk electrolyte species can easily diffuse through it and form new SEI material beneath. Less porous SEI components such as Li_2O, LiCl, and $LiClO_n$ can accumulate nearer the electrode, as they hinder the transport of electrolyte species, forming the multiphase SEI seen in Fig. 5g. The outer LiOH layer fills with electrolyte so provides a non-selective diffusion barrier to electrolyte species, but the denser, less porous inner layer may preferentially allow transport of less bulky molecules such as N_2 and H_2O rather than THF or ethanol, which may partially explain the higher faradaic efficiency observed at intermediate water concentration compared to in the dry electrolyte. The most likely causes for the improvements in faradaic efficiencies with the addition of small quantities of water that we have previously observed are the lower Li^+ conductivity in an Li_2O-rich SEI, as reported elsewhere,[13,14,22] and the finely tuned porosity of the SEI allowing selective transport of N_2 to the active surface.

During N_2 reduction, in which EtOH acts as a proton donor, LiEtO will also form as a byproduct of the protonation of Li_3N or other intermediates. Assuming water reacts with LiEtO in solution as described in reactions (2) and (3), then ethanol can be regenerated *in situ*, with the ethoxide ion acting as a shuttle of protons, and those protons ultimately being derived from water in the overall reaction:

$$N_2 + 6Li^+ + 6H_2O + 6e^- \rightarrow 2NH_3 + 6LiOH \qquad (5)$$
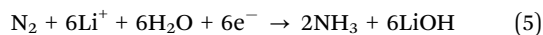
While this is a potential pathway for nitrogen reduction using water as a proton source, the fate of LiOH must be considered. LiOH makes up a significant part of SEI in water-containing electrolytes and has low solubility in THF.[59] Continuous reduction of water therefore likely results in accumulation of LiOH over time which could contribute to the poor long-term performance of the water-containing electrolyte. If an electrolyte which more readily dissolved LiOH could be developed without harming the N_2 reduction performance, the build-up of excessive solid LiOH would be prevented and increases the pH of the electrolyte. We could perhaps envisage a process by which OH^- is oxidised to water and oxygen at the anode,

similar to the anode reaction in alkaline water splitting, albeit with the challenge of avoiding the simultaneous oxidation of the electrolyte at this potential. A two-compartment cell setup using water as the proton source would be an interesting avenue for future study, though this is beyond the scope of this investigation.

Commentary on transport models

Assuming that the SEI does indeed govern the transport rates of reagents, the stark differences in SEI morphologies produced with relatively small changes in electrolyte formulations raises questions about the applicability of a general transport model to predict faradaic efficiency in the Li-mediated system. Lazouski *et al.* proposed a detailed model assuming phases of more porous and less porous SEI which act as additional diffusional boundary layers.[18] This model assumes the transport of N_2 and the proton carrier is *via* diffusion through SEI pores. This is a reasonable assumption for N_2 as a small neutral molecule, but the transport of protons may be more complex. As we have shown in this report, ethanol can form LiEtO and release a proton without direct reaction with metallic Li, and at less negative potentials than Li plating. It is possible therefore that the proton from the proton donor is released elsewhere in the SEI and transported to the active surface *via* solid-state ionic diffusion, particularly for bulkier proton donors like phenol,[28] hexanol[18] or phosphonium ions.[29] The kinetic transport model proposed earlier by Andersen *et al.*[7] predicts the faradaic efficiency to ammonia based on the transport rates of N_2 and protons to the working electrode surface, and the deposition rate of Li, assuming that reduction of N_2 and protons is instantaneous due to the high overpotentials, and makes no assumptions about the mechanisms transport for each reagent. However, this does assume that Li deposition is a competing reaction with N_2 reduction, rather than an essential stage of the mechanism. In the corrosion type mechanism now assumed in most reports,[18,32,62,63] whereby metallic Li is consumed to form Li_3N, the deposition rate of Li must be equal to or less than the transport rate of N_2 for maximum selectivity to N_2 reduction. Previous reports, including our own,[13,14,22] have attributed some improvements in faradaic efficiency under different electrolyte conditions to the suppression of excessive Li plating due to low Li^+ conductivity in the SEI. While it is reasonable to assume the rate of reduction of N_2 and protons is equal to their transport rates through the SEI, it is not necessarily the case for Li deposition if Li^+ is reformed at the active surface during Li corrosion. Under steady state N_2 reduction conditions with continuously applied current, the net diffusion rate of Li^+ from the bulk electrolyte to the electrode surface should be zero, otherwise metallic Li accumulates on the electrode or in the SEI as dead Li. We hypothesise that once the electrode surface becomes covered by electrodeposited Li, Li^+ ions are always immediately available at the active surface as long as the metallic Li is continuously corroding. The Li deposition rate is therefore limited only by the overpotential, not the Li^+ transport rate, as long as the Li deposition rate does not exceed the rate of Li corrosion (*i.e.* the transport rate of all

8424 | *Energy Environ. Sci.*, 2025, **18**, 8414–8429

This journal is © The Royal Society of Chemistry 2025

reactive species). Based on this hypothesis, and the assumption that both NH_3 formation and H_2 evolution involve consumption of Li, we offer a slightly modified prediction of the faradaic efficiency to ammonia in terms of the transport rates of N_2, r_{N_2} and protons r_H, the Li deposition rate r_{Li}, and the current losses to further SEI-forming reactions that do not consume Li, denoted l_{SEI}, which is given by eqn (6). A full derivation of this model can be found in the ESI,† as well as an alternative equation which instead assumes proton reduction to evolve H_2 does not consume Li.

$$\mathrm{FE}_{NH_3} = \begin{cases} \dfrac{6r_{N_2}}{r_{Li} + l_{SEI}} & r_{N_2} \leq \dfrac{1}{6}r_H \\ \dfrac{r_H}{r_{Li} + l_{SEI}} & r_{N_2} \geq \dfrac{1}{6}r_H \end{cases} \quad (6)$$

Following the hypothesis that Li^+ is freely available at the active surface once Li has plated, the rate of Li deposition r_{Li} can be tuned by varying the applied current density. This model predicts that the faradaic efficiency is maximised when in the proton transport-limited regime, thus avoiding excessive H_2 evolution, and the current density is optimised so that the Li deposition rate matches the limiting proton transport rate.

This interpretation further implies that any net diffusion of Li^+ from the bulk electrolyte to the working electrode surface is undesirable, as this can only result in an accumulation of Li at the surface, either as excess plated Li or dead Li. We hypothesise therefore that an ideal SEI should restrict Li^+ transport as much as possible, confining Li^+ ions to the immediate vicinity of the metallic Li layer, thus the faradaic efficiency can be maximised by matching the applied current density to the N_2 transport rate. It may be crucial to future SEI engineering to tailor to porosity to favour N_2 transport over other electrolyte species while simultaneously minimising Li^+ conductivity.

Conclusion

In this study, we combine *in situ* infrared spectroscopy measurements of SEI formation with postmortem XPS and cryo-SEM to investigate the key SEI-forming processes in Li-mediated N_2 reduction. We find that in the initial stages of SEI formation, lithium ethoxide is the dominant component, formed from the reduction of ethanol below +1.1 V *vs.* the apparent Li plating potential. The addition of small amounts of water to $LiClO_4$-based electrolytes generates highly porous LiOH from the reduction of water, observed using cryo-SEM, through which bulk electrolyte can diffuse. More passivating Li_2O forms due to the reaction between water and lithium ethoxide, which promotes the formation of dead Li but suppresses the total deposition rate of Li, and may be critical in favouring the transport of small molecules such as N_2 to the active surface over larger molecules like ethanol or THF, to which we partially attribute the increase in N_2 reduction faradaic efficiency at intermediate water concentrations. We observe qualitatively that a higher water–ethanol ratio in the electrolyte favours LiOH formation in the SEI, while a lower ratio may favour the formation of Li_2O instead. The reaction

between EtOH and water to generate Li_2O and LiOH in the SEI appears to be essential to the improvement of the water-containing $LiClO_4$ system, but will contribute to SEI formation in F-containing electrolytes through the inevitable presence of trace water. The regeneration of ethanol from LiEtO upon reaction with water raises the possibility of using water as a proton source in future studies.

Experimental methods

Full details of experimental methods can be found in the ESI,† but are briefly summarised in this section. For *in situ* FTIR measurements, the working electrode consisted of a 30 nm Cu on a 22 mm diameter hemispherical ZnSe prism. The ZnSe prims was first polished with 1 μm diamond paste and sonicated in ethanol and pure water. The Au adhesion layer was deposited onto ZnSe by an electroless plating method used for surface-enhanced infrared spectroscopy measurements.[64,65] The prism was heated to 100 °C in an oven, then transferred to a hot plate before contacting 1 ml of 10 mM $HAuCl_4$ solution onto the flat surface of the ZnSe prism at for 90 s. 30 nm of Cu was then sputtered on top of the Au. A schematic of the electrochemical cell setup used for IR measurements is shown in Fig. S1a (ESI†). The prism was pressed onto the bottom of the cell, with an exposed geometric surface area of 1.2 cm^{-2}. Pt mesh was used as the counter electrode and a Pt wire was used as a pseudo-reference electrode. The electrolytes were made inside an Ar-filled glovebox. The salts ($LiClO_4$ and $LiNTf_2$) were previously dried in a vacuum oven at 150 °C then left under vacuum in the glove box antechamber overnight. Water concentration of the electrolyte was measured using a Karl Fisher titrator. The water content of "dry" electrolyte was typically 30–50 ppm. The cell was assembled and sealed in an Ar glovebox, then brought outside for *in situ* IR measurements. N_2 or Ar was first used to purge the gas bypass line, then bubbled into the cell to saturate the electrolyte for at least 30 minutes.

The electrolytes used in this report consist of 1 M $LiClO_4$ in THF with ethanol as the proton source. Greater N_2 reduction performance has been demonstrated using various fluorinated salts like $LiNTf_2$, LiOTf and $LiBF_4$ over $LiClO_4$, however the IR absorption spectra of THF and $LiClO_4$ contain far fewer and more easily identifiable peaks, providing a clearer distinction between SEI components and background electrolyte (see Fig. S4 and S5, ESI†). Furthermore, the use of fluorinated salts caused degradation to the ZnSe prism and electrode film delamination, likely due to reaction with trace HF (Fig. S2b, ESI†). Therefore, for most of these experiments, the electrolytes consisted of 1 M $LiClO_4$ in THF/ethanol. The working electrode potential is reported relative to the apparent Li plating potential, hereafter denoted V_{Li/Li^+}. It must also be noted that partial intercalation of Li into the ZnSe prism has been observed around +0.2 V_{Li/Li^+} in battery literature,[66] however has been apparent at potentials up to +0.5 V_{Li/Li^+} in these experiments, which can obscure the onset of true metallic Li plating (Fig. S2a, ESI†), so the apparent Li plating potential

alone cannot be used as an accurate reference potential in this setup. The Li plating potential *vs.* Pt wire in each experiment has therefore been estimated retrospectively using the same cell setup and an LFP reference electrode. As a result, some of the FTIR measurements are not made up to the true onset of Li plating. It should also be noted that the true Li plating potential will shift slightly depending on the electrolyte.[67,68] For each *in situ* FTIR experiment, a background IR spectrum was taken at the initial open circuit potential (OCP) in each experiment (normally around +3.4 V_{Li/Li^+}), so all peaks in subsequent figures show the differences in IR absorption *vs.* the clean electrode surface at the initial OCP.

Most ATR-FTIR measurements were made using a Thermo Fisher iS50, and some measured with Bruker Invenio spectrometer equipped with a VEEMAX variable angle accessory, with an angle of incidence of 70°. Both spectrometers were equipped with a liquid nitrogen-cooled mercury cadmium telluride (MCT) detector. In each experiment, the potential was held at open circuit potential for at least 30 minutes. A background IR spectrum was then taken at open circuit potential immediately before the start of the first potential scan.

Samples for postmortem SEM and XPS measurements were made in a single compartment glass cell (Fig. S1c, ESI†) inside an Ar-filled glove box. 1 cm^2 Mo or Cu foil was used as the working electrode with Cu wire as the current collector. The counter and reference were Pt mesh and Pt wire respectively, as with the FTIR cell. Following an initial LSV to the onset of Li plating, 10C of charge was passed at −2 mA cm^{-2}. Electrodes were stored in the Ar glove box between preparation and measurement, and heat sealed into an Ar-filled bag to be transported to the microscope. SEM images were made under cryogenic conditions (around −165 °C) and SEI cross-sections were cut using focused ion beam (FIB) milling (see ESI,† for full details). A protective layer of Pt was deposited to reduce curtaining as an artefact during FIB milling. This Pt layer is manifested as a white band in the micrographs in Fig. 5.

Author contributions

FTIR measurements: M. S., J. R.; FTIR thin film fabrication: M. S., J. R., C. T., A. M.; SEM measurements: O. W., J. O. D., M. C.; XPS measurements: O. W.; interpretation of FTIR data: M. S., J. R., Y. Katayama; interpretation of SEM and XPS: M. S., O. W., Y. Katayama., C. B.; making figures: M. S., C. B., Y. Katayama; FTIR cell design: Y. K., Y. K., M. S., J. R.; project supervision: I. E. L. S., M. T., Y. Katayama, Y. Y.; preparing manuscript: M. S.; reviewing manuscript: all authors. Editing and finalising manuscript: M. S., Y. Katayama.

Conflicts of interest

Olivia Westhead reports employment at NitroVolt ApS. The other authors declare no conflicts of interest.

Data availability

Data supporting this article, including full FTIR spectra, reference spectra and XPS measurements, are included in the ESI.†

References

1 J. G. Chen, R. M. Crooks and L. C. Seefeldt, *et al.*, Beyond fossil fuel–driven nitrogen transformations, *Science*, 2018, **360**, eaar6611, DOI: **10.1126/science.aar6611**.

2 S. Mingolla and L. Rosa, Low-carbon ammonia production is essential for resilient and sustainable agriculture, *Nat. Food*, 2025, **6**(6), 610–621, DOI: **10.1038/s43016-025-01125-y**.

3 S. Z. Andersen, V. Čolić and S. Yang, *et al.*, A rigorous electrochemical ammonia synthesis protocol with quantitative isotope measurements, *Nature*, 2019, **570**(7762), 504–508, DOI: **10.1038/s41586-019-1260-x**.

4 O. Westhead, J. Barrio and A. Bagger, *et al.*, Near ambient N$_2$ fixation on solid electrodes versus enzymes and homogeneous catalysts, *Nat. Rev. Chem.*, 2023, **7**(3), 184–201, DOI: **10.1038/s41570-023-00462-5**.

5 A. Tsuneto, A. Kudo and T. Sakata, Efficient Electrochemical Reduction of N$_2$ to NH$_3$ Catalyzed by Lithium, *Chem. Lett.*, 1993, (5), 851–854, DOI: **10.1246/cl.1993.851**.

6 A. Tsuneto, A. Kudo and T. Sakata, Lithium-mediated electrochemical reduction of high pressure N$_2$ to NH$_3$, *J. Electroanal. Chem.*, 1994, **367**, 183–188.

7 S. Z. Andersen, M. J. Statt and V. J. Bukas, *et al.*, Increasing stability, efficiency, and fundamental understanding of

8426 | *Energy Environ. Sci.*, 2025, **18**, 8414–8429

This journal is © The Royal Society of Chemistry 2025

lithium-mediated electrochemical nitrogen reduction, *Energy Environ. Sci.*, 2020, **13**(11), 4291–4300, DOI: **10.1039/d0ee02246b**.

8 J. A. Schwalbe, M. J. Statt and C. Chosy, *et al.*, A Combined Theory-Experiment Analysis of the Surface Species in Lithium-Mediated NH₃ Electrosynthesis, *ChemElectroChem*, 2020, **7**(7), 1542–1549, DOI: **10.1002/celc.201902124**.

9 P. V. Cherepanov, M. Krebsz, R. Y. Hodgetts, A. N. Simonov and D. R. MacFarlane, Understanding the Factors Determining the faradaic Efficiency and Rate of the Lithium Redox-Mediated N₂ Reduction to Ammonia, *J. Phys. Chem. C*, 2021, **125**(21), 11402–11410, DOI: **10.1021/acs.jpcc.1c02494**.

10 R. Sažinas, S. Z. Andersen and K. Li, *et al.*, Towards understanding of electrolyte degradation in lithium-mediated non-aqueous electrochemical ammonia synthesis with gas chromatography–mass spectrometry, *RSC Adv.*, 2021, **11**(50), 31487–31498, DOI: **10.1039/d1ra05963g**.

11 S. Li, Y. Zhou and K. Li, *et al.*, Electrosynthesis of ammonia with high selectivity and high rates via engineering of the solid–electrolyte interphase, *Joule*, 2022, **6**(9), 2083–2101, DOI: **10.1016/j.joule.2022.07.009**.

12 H. L. Du, M. Chatti and R. Y. Hodgetts, *et al.*, Electroreduction of nitrogen with almost 100% current-to-ammonia efficiency, *Nature*, 2022, **609**(7928), 722–727, DOI: **10.1038/s41586-022-05108-y**.

13 K. Li, S. Z. Andersen and M. J. Statt, *et al.*, Enhancement of lithium-mediated ammonia synthesis by addition of oxygen, *Science*, 2021, **374**(6575), 1593–1597, DOI: **10.1126/science.abl4300**.

14 R. Sažinas, K. Li and S. Z. Andersen, *et al.*, Oxygen-Enhanced Chemical Stability of Lithium-Mediated Electrochemical Ammonia Synthesis, *J. Phys. Chem. Lett.*, 2022, **13**(20), 4605–4611, DOI: **10.1021/acs.jpclett.2c00768**.

15 E. Peled, The Electrochemical Behavior of Alkali and Alkaline Earth Metals in Nonaqueous Battery Systems—The Solid Electrolyte Interphase Model, *J. Electrochem. Soc.*, 1979, **126**(12), 2047–2051, DOI: **10.1149/1.2128859**.

16 J. B. Goodenough and Y. Kim, Challenges for rechargeable Li batteries, *Chem. Mater.*, 2010, **22**(3), 587–603, DOI: **10.1021/cm901452z**.

17 K. Steinberg, X. Yuan and C. K. Klein, *et al.*, Imaging of nitrogen fixation at lithium solid electrolyte interphases via cryo-electron microscopy, *Nat. Energy*, 2023, **8**(2), 138–148, DOI: **10.1038/s41560-022-01177-5**.

18 N. Lazouski, K. J. Steinberg, M. L. Gala, D. Krishnamurthy, V. Viswanathan and K. Manthiram, Proton Donors Induce a Differential Transport Effect for Selectivity toward Ammonia in Lithium-Mediated Nitrogen Reduction, *ACS Catal.*, 2022, **12**(9), 5197–5208, DOI: **10.1021/acscatal.2c00389**.

19 E. J. McShane, V. A. Niemann and P. Benedek, *et al.*, Quantifying Influence of the Solid–Electrolyte Interphase in Ammonia Electrosynthesis, *ACS Energy Lett.*, 2023, **8**(10), 4024–4032, DOI: **10.1021/acsenergylett.3c01534**.

20 S. J. Blair, M. Doucet and V. A. Niemann, *et al.*, Combined, time-resolved, in situ neutron reflectometry and X-ray diffraction analysis of dynamic SEI formation during electrochemical N₂ reduction, *Energy Environ. Sci.*, 2023, **16**(8), 3391–3406, DOI: **10.1039/d2ee03694k**.

21 A. R. Singh, B. A. Rohr, M. J. Statt, J. A. Schwalbe, M. Cargnello and J. K. Nørskov, Strategies toward Selective Electrochemical Ammonia Synthesis, *ACS Catal.*, 2019, **9**(9), 8316–8324, DOI: **10.1021/acscatal.9b02245**.

22 M. Spry, O. Westhead and R. Tort, *et al.*, Water Increases the faradaic Selectivity of Li-Mediated Nitrogen Reduction, *ACS Energy Lett.*, 2023, **8**(2), 1230–1235, DOI: **10.1021/acsenergylett.2c02792**.

23 R. Tort, A. Bagger and O. Westhead, *et al.*, Searching for the Rules of Electrochemical Nitrogen Fixation, *ACS Catal.*, 2023, **13**(22), 14513–14522, DOI: **10.1021/acscatal.3c03951**.

24 H. L. Du, K. Matuszek and R. Y. Hodgetts, *et al.*, The chemistry of proton carriers in high-performance lithium-mediated ammonia electrosynthesis, *Energy Environ. Sci.*, 2023, **16**(3), 1082–1090, DOI: **10.1039/D2EE03901J**.

25 N. Lazouski, Z. J. Schiffer, K. Williams and K. Manthiram, Understanding Continuous Lithium-Mediated Electrochemical Nitrogen Reduction, *Joule*, 2019, **3**(4), 1127–1139, DOI: **10.1016/j.joule.2019.02.003**.

26 O. Westhead, M. Spry and A. Bagger, *et al.*, The role of ion solvation in lithium mediated nitrogen reduction, *J. Mater. Chem. A*, 2022, **11**(24), 12746–12758, DOI: **10.1039/d2ta07686a**.

27 J. Bjarke Valbæk Mygind, J. B. Pedersen and K. Li, *et al.*, Is Ethanol Essential for the Lithium-Mediated Nitrogen Reduction Reaction?, *ChemSusChem*, 2023, **16**(22), e202301011, DOI: **10.1002/cssc.202301011**.

28 X. Fu, A. Xu and J. B. Pedersen, *et al.*, Phenol as proton shuttle and buffer for lithium-mediated ammonia electrosynthesis, *Nat. Commun.*, 2024, **15**, 2417, DOI: **10.1038/s41467-024-46803-w**.

29 B. H. R. Suryanto, K. Matuszek and J. Choi, *et al.*, Nitrogen reduction to ammonia at high efficiency and rates based on a phosphonium proton shuttle, *Science*, 2021, **372**(6547), 1187–1191, DOI: **10.1126/science.abg2371**.

30 R. Tort, O. Westhead, J. O. Douglas, *et al.*, The Role of Ethanol in Lithium-Mediated Nitrogen Reduction, *ChemRxiv*, 2025, preprint, DOI: **10.26434/chemrxiv-2025-q3fjz**.

31 W. Chang, A. Jain, F. Rezaie and K. Manthiram, Lithium-mediated nitrogen reduction to ammonia via the catalytic solid–electrolyte interphase, *Nat. Catal.*, 2024, **7**(3), 231–241, DOI: **10.1038/s41929-024-01115-6**.

32 X. Fu, J. B. Pedersen and Y. Zhou, *et al.*, Continuous-flow electrosynthesis of ammonia by nitrogen reduction and hydrogen oxidation, *Science*, 2023, **379**(6633), 707–712, DOI: **10.1126/science.adf4403**.

33 X. Fu, S. Li, N. H. Deissler, J. B. V. Mygind, J. Kibsgaard and I. Chorkendorff, Effect of Lithium Salt on Lithium-Mediated Ammonia Synthesis, *ACS Energy Lett.*, 2024, **9**(8), 3790–3795, DOI: **10.1021/acsenergylett.4c01655**.

34 D. Krishnamurthy, N. Lazouski, M. L. Gala, K. Manthiram and V. Viswanathan, Closed-Loop Electrolyte Design for Lithium-Mediated Ammonia Synthesis, *ACS Cent. Sci.*, 2021, **7**(12), 2073–2082, DOI: **10.1021/acscentsci.1c01151**.

This journal is © The Royal Society of Chemistry 2025

Energy Environ. Sci., 2025, **18**, 8414–8429 | **8427**

35 A. Mangini, J. B. V. Mygind and S. G. Ballesteros, et al., Multivariate Approaches Boosting Lithium-Mediated Ammonia Electrosynthesis in Different Electrolytes, *Angew. Chem., Int. Ed.*, 2025, **64**, e202416027, DOI: **10.1002/anie.202416027**.

36 J. Hyung Kim, J. E. Cha and H. K. Ju, et al., Utilizing water as a proton source for sustainable Li-mediated electrochemical ammonia synthesis, *Chem. Eng. J.*, 2024, 497, DOI: **10.1016/j.cej.2024.154644**.

37 S. J. Blair, M. Doucet and J. F. Browning, et al., Lithium-Mediated Electrochemical Nitrogen Reduction: Tracking Electrode-Electrolyte Interfaces via Time-Resolved Neutron Reflectometry, *ACS Energy Lett.*, 2022, **7**(6), 1939–1946, DOI: **10.1021/acsenergylett.1c02833**.

38 Y. Yamada, K. Furukawa and K. Sodeyama, et al., Unusual Stability of Acetonitrile-Based Superconcentrated Electrolytes for Fast-Charging Lithium-Ion Batteries, *J. Am. Chem. Soc.*, 2014, **136**(13), 5039–5046, DOI: **10.1021/ja412807w**.

39 B. Cadioli, E. Gallinella, C. Coulombeau, H. Jobic and G. Berthier, Geometric structure and vibrational spectrum of tetrahydrofuran, *J. Phys. Chem.*, 1993, **97**(30), 7844–7856, DOI: **10.1021/j100132a010**.

40 J. S. Seo, B. S. Cheong and H. G. Cho, Solvation of $LiClO_4$ and $NaClO_4$ in deuterated acetonitrile studied by means of infrared and Raman spectroscopy, *Spectrochim. Acta, Part A*, 2002, **58**(8), 1747–1756, DOI: **10.1016/S1386-1425(01)00636-9**.

41 M. H. Brooker and J. B. Bates, Raman and infrared spectral studies of anhydrous Li_2CO_3 and Na_2CO_3, *J. Chem. Phys.*, 1971, **54**(11), 4775–4787, DOI: **10.1063/1.1674754**.

42 J. Y. Liang, S. R. Shin, S. H. Lee and D. S. Lee, Characteristics of self-healable copolymers of styrene and eugenol terminated polyurethane prepolymer, *Polymers*, 2019, **11**(10), 1674, DOI: **10.3390/polym11101674**.

43 S. Nakahama, S. Hino and N. Yamazaki, Electrolytic Polymerization of Tetrahydrofuran, *Polym. J.*, 1971, **2**(1), 56–61, DOI: **10.1295/polymj.2.56**.

44 A. N. Dey and E. J. Rudd, Electroinitiated Polymerization of Tetrahydrofuran, *J. Electrochem. Soc.*, 1974, **121**(10), 1294, DOI: **10.1149/1.2401671**.

45 S. Li, Y. Zhou and X. Fu, et al., Long-term continuous ammonia electrosynthesis, *Nature*, 2024, **629**(8010), 92–97, DOI: **10.1038/s41586-024-07276-5**.

46 D. Strmcnik, I. E. Castelli and J. G. Connell, et al., Electrocatalytic transformation of HF impurity to H_2 and LiF in lithium-ion batteries, *Nat. Catal.*, 2018, **1**(4), 255–262, DOI: **10.1038/s41929-018-0047-z**.

47 M. Martins, D. Haering and J. G. Connell, et al., Role of Catalytic Conversions of Ethylene Carbonate, Water, and HF in Forming the Solid–Electrolyte Interphase of Li-Ion Batteries, *ACS Catal.*, 2023, **13**(13), 9289–9301, DOI: **10.1021/acscatal.3c01531**.

48 I. E. Castelli, M. Zorko and T. M. Østergaard, et al., The role of an interface in stabilizing reaction intermediates for hydrogen evolution in aprotic electrolytes, *Chem. Sci.*, 2020, **11**(15), 3914–3922, DOI: **10.1039/C9SC05768D**.

49 M. Osawa, M. Tsushima, H. Mogami, G. Samjeské and A. Yamakata, Structure of Water at the Electrified Platinum−Water Interface: A Study by Surface-Enhanced Infrared Absorption Spectroscopy, *J. Phys. Chem. C*, 2008, **112**(11), 4248–4256, DOI: **10.1021/jp710386g**.

50 M. Takeuchi, R. Kurosawa, J. Ryu and M. Matsuoka, Hydration of LiOH and LiCl-Near-Infrared Spectroscopic Analysis, *ACS Omega*, 2021, **6**(48), 33075–33084, DOI: **10.1021/acsomega.1c05379**.

51 G. Weber, E. Sciora and J. Guichard, et al., Investigation of hydrolysis of lithium oxide by thermogravimetry, calorimetry and in situ FTIR spectroscopy, *J. Therm. Anal. Calorim.*, 2018, **132**(2), 1055–1064, DOI: **10.1007/s10973-017-6943-7**.

52 S. T. Liu, H. Y. Ku, C. L. Huang and C. C. Hu, Improvements in Li deposition and stripping induced by Cu(111) nanotwinned columnar grains, *Electrochim. Acta*, 2022, 430, DOI: **10.1016/j.electacta.2022.141011**.

53 Y. Gu, H. Y. Xu and X. G. Zhang, et al., Lithiophilic Faceted Cu(100) Surfaces: High Utilization of Host Surface and Cavities for Lithium Metal Anodes, *Angew. Chem., Int. Ed.*, 2019, **58**(10), 3092–3096, DOI: **10.1002/anie.201812523**.

54 Y. Jeon, D. Shin, K. Yong and Y. J. Hwang, Enhancing Ammonia Production by Ag Incorporation in Li-Mediated Nitrogen Reduction Reactions, *ACS Energy Lett.*, 2024, **9**(8), 4147–4152, DOI: **10.1021/acsenergylett.4c01438**.

55 J. S. Nowick and G. Lutterbach, *Lithium Chloride, Encyclopedia of Reagents for Organic Synthesis*, John Wiley & Sons, Ltd, 2001, DOI: **10.1002/047084289X.rl076**.

56 D. Wynn, The solubility of alkali-metal fluorides in nonaqueous solvents with and without crown ethers, as determined by flame emission spectrometry, *Talanta*, 1984, **31**(11), 1036–1040, DOI: **10.1016/0039-9140(84)80244-1**.

57 K. Li, S. G. Shapel and D. Hochfilzer, et al., Increasing Current Density of Li-Mediated Ammonia Synthesis with High Surface Area Copper Electrodes, *ACS Energy Lett.*, 2022, **7**(1), 36–41, DOI: **10.1021/acsenergylett.1c02104**.

58 B. Burrows and S. Kirkland, Electrochemical Behavior of H_2O in Nonaqueous Electrolyte, *J. Electrochem. Soc.*, 1968, **115**(11), 1164, DOI: **10.1149/1.2410930**.

59 D. Aurbach and O. Chusid, The use of in situ Fourier-transform infrared spectroscopy for the study of surface phenomena on electrodes in selected lithium battery electrolyte solutions, *J. Power Sources*, 1997, **68**(2), 463–470, DOI: **10.1016/S0378-7753(97)02622-0**.

60 K. Tasaki and S. J. Harris, Computational Study on the Solubility of Lithium Salts Formed on Lithium Ion Battery Negative Electrode in Organic Solvents, *J. Phys. Chem. C*, 2010, **114**(17), 8076–8083, DOI: **10.1021/jp100013h**.

61 J. Jones, M. Anouti, M. Caillon-Caravanier, P. Willmann, P. Y. Sizaret and D. Lemordant, Solubilization of SEI lithium salts in alkylcarbonate solvents, *Fluid Phase Equilib.*, 2011, **305**(2), 121–126, DOI: **10.1016/j.fluid.2011.03.007**.

62 X. Cai, C. Fu and H. Iriawan, et al., Lithium-mediated electrochemical nitrogen reduction: Mechanistic insights to enhance performance, *iScience*, 2021, **24**(10), 103105, DOI: **10.1016/j.isci.2021.103105**.

8428 | *Energy Environ. Sci.*, 2025, **18**, 8414–8429

This journal is © The Royal Society of Chemistry 2025

63 L. M. Azofra, J. M. Doña-Rodríguez, D. R. MacFarlane and A. N. Simonov, Mechanism of the N_2 Cleavage Promoted by Lithium *vs.* Other Alkali and Alkaline-Earth Metals, *J. Phys. Chem. C*, 2025, **129**(2), 1198–1205, DOI: **10.1021/acs.jpcc.4c07438**.

64 C. Tseng, A. K. Pennathur, D. Blauth, N. Salazar and J. M. Dawlaty, Direct Determination of Plasmon Enhancement Factor and Penetration Depths in Surface Enhanced IR Absorption Spectroscopy, *Langmuir*, 2023, **39**(9), 3179–3184, DOI: **10.1021/acs.langmuir.2c02254**.

65 W. J. Bao, J. Li and J. Li, *et al.*, Au/ZnSe-Based Surface Enhanced Infrared Absorption Spectroscopy as a Universal Platform for Bioanalysis, *Anal. Chem.*, 2018, **90**(6), 3842–3848, DOI: **10.1021/acs.analchem.7b04505**.

66 X. Cao, A. Li, Y. Yang and J. Chen, ZnSe nanoparticles dispersed in reduced graphene oxides with enhanced electrochemical properties in lithium/sodium ion batteries, *RSC Adv.*, 2018, **8**(45), 25734–25744, DOI: **10.1039/C8RA03479F**.

67 R. Tort, O. Westhead and M. Spry, *et al.*, Nonaqueous Li-Mediated Nitrogen Reduction: Taking Control of Potentials, *ACS Energy Lett.*, 2023, **8**(2), 1003–1009, DOI: **10.1021/acsenergylett.2c02697**.

68 E. J. McShane, P. Benedek and V. A. Niemann, *et al.*, A Versatile $Li_{0.5}FePO_4$ Reference Electrode for Nonaqueous Electrochemical Conversion Technologies, *ACS Energy Lett.*, 2023, **8**(1), 230–235, DOI: **10.1021/acsenergylett.2c02190**.

This journal is © The Royal Society of Chemistry 2025

Energy Environ. Sci., 2025, **18**, 8414–8429 | 8429